Spring 2009

A new method of threshold and gradient optimization using class uncertainty theory and its quantitative analysis

Yinxiao Liu
University of Iowa

A NEW METHOD OF THRESHOLD AND GRADIENT OPTIMIZATION USING CLASS UNCERTAINTY THEORY AND ITS QUANTITATIVE ANALYSIS

by

Yinxiao Liu

A thesis submitted in partial fulfillment
of the requirements for the Master of
Science degree in Electrical and Computer Engineering
in the Graduate College of
The University of Iowa

May 2009

Thesis Supervisor: Associate Professor Punam K. Saha

Graduate College
The University of Iowa
Iowa City, Iowa

CERTIFICATE OF APPROVAL

_____

MASTER'S THESIS

_____

This is to certify that the Master's thesis of

Yinxiao Liu

has been approved by the Examining Committee
for the thesis requirement for the Master of Science
degree in Electrical and Computer Engineering at the May 2009 graduation.

Thesis Committee: _____
Punam K. Saha, Thesis Supervisor

_____
Erwei Bai

_____
Xiaodong Wu

ACKNOWLEDGMENTS

First of all, I would like to give my most sincere thanks to my advisor Professor Punam K. Saha for his patient help and guidance on my research. I would like to thank Professor Milan Sonka, and Professor Joseph Reinhardt for their advice for my work. Also I would like to give my thanks to Qi Song, Xin Dou for their help as my friends and seniors. Special thanks to Lu Bi for her help on my work and my daily life. In the end, I want to thanks all the faculties, staffs and students at IIBI for their intuitive lectures and help.

ABSTRACT

The knowledge of thresholding and gradient at different tissue interfaces is of paramount interest in image segmentation and other imaging methods and applications. Most thresholding and gradient selection methods primarily focus on image histograms and therefore, fail to harness the information generated by intensity patterns in an image. We present a new thresholding and gradient optimization method which accounts for spatial arrangement of intensities forming different objects in an image. Specifically, we recognize object class uncertainty, a histogram-based feature, and formulate an energy function based on its correlation with image gradients that characterizes the objects and shapes in a given image. Finally, this energy function is used to determine optimum thresholds and gradients for various tissue interfaces. The underlying theory behind the method is that objects manifest themselves with fuzzy boundaries in an acquired image and that, in a probabilistic sense; intensities with high class uncertainty are associated with high image gradients generally indicating object/tissue interfaces. The new method simultaneously determines optimum values for both thresholds and gradient parameters at different object/tissue interfaces. The method has been applied on several 2D and 3D medical image data sets and it has successfully determined both thresholds and gradients for different tissue interfaces even when some of the thresholds are almost impossible to locate in their histograms. The accuracy and reproducibility of the method has been examined using 3D multi-row detector computed tomography images of two cadaveric ankles each scanned thrice with repositioning the specimen between two scans.

TABLE OF CONTENTS

ACKNOWLEDGEMENT II

ABSTRACT III

LIST OF TABLES V

LIST OF FIGURES VI

CHAPTER ONE INTRODUCTION 1

1.1 Image Segmentation and Thresholding 1
1.2 Optimum and Automatic Thresholding 2
1.3 Outline 4

CHAPTER TWO THEORY 6

2.1 Intensity-based Class Uncertainty 9
2.2 Energy Surface and Optimun Thresholding 11

CHAPTER THREE METHODS AND EXPERIMENTAL SETTING 13

3.1 Methods 13
3.2 Experimental Setting 17
3.3.1 CT image description 17
3.3.2 MR phantom image description 18
3.3.3 Error estimation 18

CHAPTER FOUR RESULTS AND DISCUSSION 20

4.1 Results 20
4.1.1 Qualification analysis 20
4.1.2 Comparison with Otsu's thresholding method 24
4.1.3 Accuracy analysis on MR phantom images 26
4.1.4 Accuracy analysis on 3D CT ankle images 28
4.1.5 Reproducibility analysis on 3D CT ankle images 29
4.2 Discussion 29

REFERENCES 30

LIST OF TABLES

Table 1 Error measures of thresholding for different T1-weighted MR phantom images and tissue regions. 27

Table 2 Error measures of thresholding for T images of two ankle specimens.....28

Table 3 Preliminary results of reproducibility analysis using MDCT repeat scans of a cadaveric ankle specimen.....28

LIST OF FIGURES

Figure. 1 Illustration of the relation between thresholding and object class uncertainty values for a two class problem.....7

Figure. 2 An illustration of the class uncertainty theory. (a) A 2D image slice from a CT image of a patient's abdomen. (b) Image intensity histogram for (a) with three marks for thresholds $t1$, $t2$ and $t3$. (c) The region computed by setting the threshold at $t1$. (d) The class uncertainty map computed for threshold at $t1$ clearly depicting the tissue interface of lever and other soft tissues. (e,f) Same as (c,d) but for bone region with threshold at $t3$. (g,h) Same as (c,d) but using a threshold $t2$indicating no meaningful region. Note that the class-uncertainty map in (h) fails to indicate any tissue interface and spells over the entire soft tissue region. 8

Figure. 3 An illustration of intrinsic basins. 16

Figure. 4 A graphical description of the error function defining up the merit of a selected threshold s; here, t denotes the true threshold. Essentially, it computes the difference of the number of pixels/voxels, (the yellow region), normalized by image size. 19

Figure. 5 Results of application of the method on an image slice from a CT data of lower abdomen. (a) Original CT image slice. (b) Thresholded regions in different colors as applied on the original image. (c) Same as (b) but applied on a smoothed image. (d) Thresholded regions in different colors as applied on the original image. (c) Same as (b) but applied on a smoothed image. (d) Thresholds shown in image histogram with red lines. (e) The energy surface/function with valley lines shown in red and pits indicated by red circles. (f-h) Object class uncertainty maps at different optimum thresholds. Note that the object class uncertainty image highlights different tissue interface at different optimum thresholds. 21

Figure. 6 Same as Figure. 5, but for a CT image slice of abdomen.....22

Figure. 7 Same as Figure. 5, but for a 3D CT image of ankle. 23

Figure. 8 Automatic thresholding compare with Otsu's thresholding method. (a) Original lena image. (b) Automatic thresholding result. (c) Otsu's threhsolding method with same number of thresholds 25

Figure. 9 MRI T1 phantoms with different noise levels and their segmented results. (a) no noise. (b) 1% noise. (c) 3% noise. (d) 5% noise. (e)-(g) segmented result for different noise levels. 26

CHAPTER ONE

INTRODUCTION

1.1 Image Segmentation and Thresholding

Over the last few decades, multi-layered extraction of knowledge embedded in two- and higher-dimensional images has remained a front line research topic [1-7]. In particular availability of a wide spectrum of medical imaging techniques [8] including MR, ultrasound, CT, PET, and X- and γ-rays have further intensified the image processing needs for computerized extraction of knowledge from the huge image data sets produced. Segmentation has remained a salient task in most imaging applications, in particular, those involving object classification, geometry, shape, and motion analysis. Some other imaging steps including interpolation, filtering and registration may also be significantly improved with the *a priori* knowledge of objects and shapes. With all these reasons, defining objects in a precise and effective way becomes vital for any computerized imaging applications, and this is usually referred as image segmentation.

Pal and Pal [9] reviewed various methods for gray-level image segmentation. Despite major advances in image segmentation methods [10-15], often, yielding acceptable results, thresholding is undoubtedly one of the most popular segmentation approaches, because of its simplicity and relative robustness. Usually the gray levels of pixels belonging to the object are substantially different from the gray levels of those belonging to the background, so by thresholding at proper thresholds, it is quite easy and effective to separate object from background. The output of thresholding operation is a binary image whose one state will indicate the foreground objects, that is, printed text, a

legend, a target, defective part of a material, etc., while the complementary state will correspond to the background. Depending on the application, the foreground can be represented by gray-level 0, that is, black as for text, and the background by the highest luminance for the document paper, which is 255 in 8-bit images, or conversely the foreground by white and the background by black. Various factors, such as nonstationary and correlated noise, ambient illumination, busyness of gray levels within the object and its background, inadequate contrast, and object size not commensurate with the scene, complicate the thresholding potation. Finally, the lack of object measure to assess the performance of various thresholding algorithms, and the difficulty of extensive testing in a task-oriented environment, are other major handicaps [43].

1.2 Optimum and Automatic thresholding

Often, optimum thresholding along with gradient selection are hidden problems in many advanced segmentation approaches, or, at least would help toward automation of such methods. For example, the knowledge of average tissue intensity along with the gradient at different tissue interface should bring momentous improvements in different boundary-, region- and shape-based segmentation approaches.

Automatic selection of a robust and accurate threshold has remained a challenge in image segmentation. Many methods for automatic threshold selection have been reported [16-35] over the past five decades. In late 80’s, Sahoo et al. [16] published a survey of optimum thresholding methods while Lee et al. [17] reported the results of a comparative study of thresholding methods. Glasbely [18] published the results of another comparative study involving eleven histogram-based thresholding algorithms. Among the early works on automatic thresholding, Prewitt and Mendelson [19] suggested

using the valleys of the histogram, while Doyle [20] advocated the choice of the median. Otsu [21] developed a thresholding method maximizing the between-class variance. Tsai [24] proposed a choice of the threshold at which resulting binary images have identical first three moments.

Later works on threshing have utilized entropy of the original and thresholded images to construct an optimization criterion. For example, Pun's method [25] maximizes the upper bound of the *a posteriori* entropy of the histogram. Wong and Sahoo's method [26] selects the optimum threshold that maximizes the *a posteriori* entropy subject to certain inequality constraints characterizing the uniformity and shape of the segmented regions. Pal and Pal's method [27] utilized the joint probability distribution of the neighboring pixels which they further modified28 with a new definition of entropy. Kapur et al. [29] proposed a thresholding method maximizing the sum of entropies of the segmented regions and a similar method was reported by Abutaleb [30] that maximizes the 2D entropy. The method by Brink [31] maximizes the sum of the entropies computed from two autocorrelation functions of the thresholded image histograms. Li and Lee's method [32] minimizes relative cross entropy or Kullback-Leibler distance between the original and thresholded images. Kitler and Illingworth33 developed a thresholding method minimizing segmentation errors derived using an information-theoretic approach, while Dunn et al.'s method [34] used a uniform error criterion. Leung and Lam [35] developed a method that maximizes segmented image information derived using an information-theoretic approach and demonstrated that their method is better than the methods based on minimum and uniform errors [33, 34].

Although, Wong and Sahoo [26] and Pal and Pal [27, 28] incorporated some spatial image information in their methods, others are mostly histogram-based techniques. One common shortcoming of a purely histogram-based approach is that it does not utilize the significant amount of information embedded in the spatial distribution of intensities and in image morphology. Often, it is not possible for a human observer to select a threshold in an image just from its histogram without seeing the original image. On the other hand, the image may contain clear partitions of different object or tissue regions and it may only be a trivial task to select the threshold from the image. This observation inspired us to develop a method that directly makes use of impressions created on the image by different object/tissue interfaces. In our previous work [36], we introduced the idea of class-uncertainty and demonstrated its relation with interfaces of multiple objects or tissue regions. The method captures the fuzziness caused by blurring or the ubiquitous partial voluming effect introduced by an imaging device and utilizes this fuzziness in optimum thresholding by relating it with class uncertainty. Class uncertainty is byproduct information of object classification and it's often ignored in the context of computer vision and imaging applications. In our previous work, it was demonstrated that high class-uncertainty, commonly associated with intermediate intensity values on the histogram between two object classes, appear in the vicinity of object or tissue interfaces in an image. This observation provides a unique theory of relating histogram based information with image derived features.

1.3 Outline

Although, based on the above idea, an optimum threshold selection method was developed in our previous work, it suffers from two limitations – (1) an ad hoc rank-

based approach was adopted for normalizing the image gradient feature which may shift the fulcrum as the amount of edginess varies across images and (2) fails to capture varying intensity contrasts at different tissue interfaces. Here, we solve these two major problems by simultaneously optimizing the gradients and threshold. The new method needs no *a priori* assumption on image gradient values and yields the optimum image gradients for different tissue interfaces along with the optimum thresholds.

In Chapter 2, we discuss the class uncertainty theory and how it is combined with gradient optimization. In Chapter 3, we show in detail how we implement our method and the experimental settings. In Chapter 4, we present the qualification result of our method, and the quantitative analysis consisting of both accuracy and reproducibility.

CHAPTER TWO

THEORY

In the context of thresholding or classification, we mostly care about the class or the region to which an image point is partitioned and, often, ignore an important piece of information related to the confidence level or uncertainty associated with the classification; we will refer to it as class-uncertainty. For example, considering the object and background intensity distribution illustrated in Figure. 1, a point with either intensity t_1 or $t_2$will be classified as an object point. However, the class-uncertainties in the two cases are significantly different. In an original work, Saha and Udupa [36] derived a measure of class-uncertainty in terms of *a priori* object and background intensity distributions and the density function. Also, they demonstrated the relation class-uncertainty and image-derived features. The following postulate proposed in [36] governs the relation between class-uncertainty and image-derived features.

Postulate A. *In an image with fuzzy boundaries, under optimum partitioning of object classes, intensities with high class uncertainty appear around object boundaries.*

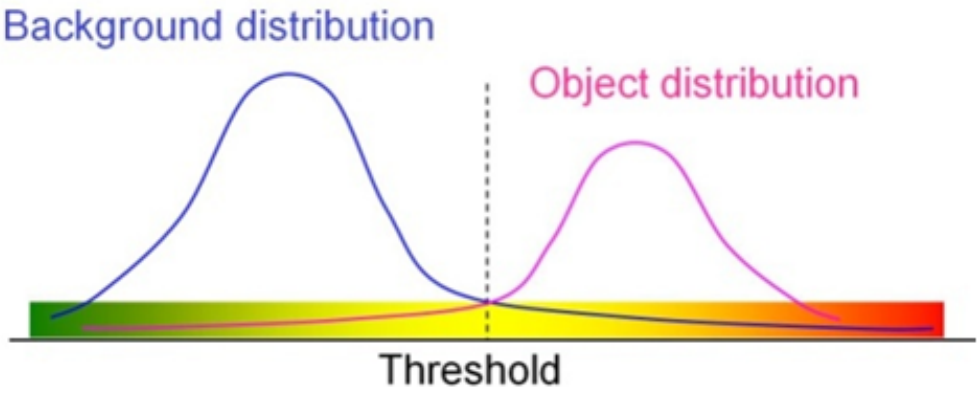

Figure. 1 Illustration of the relation between thresholding and object class uncertainty values for a two class problem.

Although it is difficult to prove or disprove the postulate because of its nature, its validity may be justified on real-life images. Let us consider a computed tomography (CT) image of abdomen (see Figure. 2(a)) depicting several tissue regions with different intensity values. To illustrate the basic idea of the class uncertainty theory, let us manually pick three thresholds on the intensity histogram of the CT image (see Figure. 2(b)) of which two are expected to separate meaningful tissue regions (see Figure. 2(c,g)) while the other is intentionally selected not to represent a meaningful tissue region (see Figure. 2(e)). Interestingly, the class-uncertainty images (see Figure. 2(d) and (h)) for the two meaningful thresholds clearly portray corresponding tissue interfaces while the class-uncertainty map for the wrong threshold fails to depict any visible tissue interface (see Figure. 2(f)).

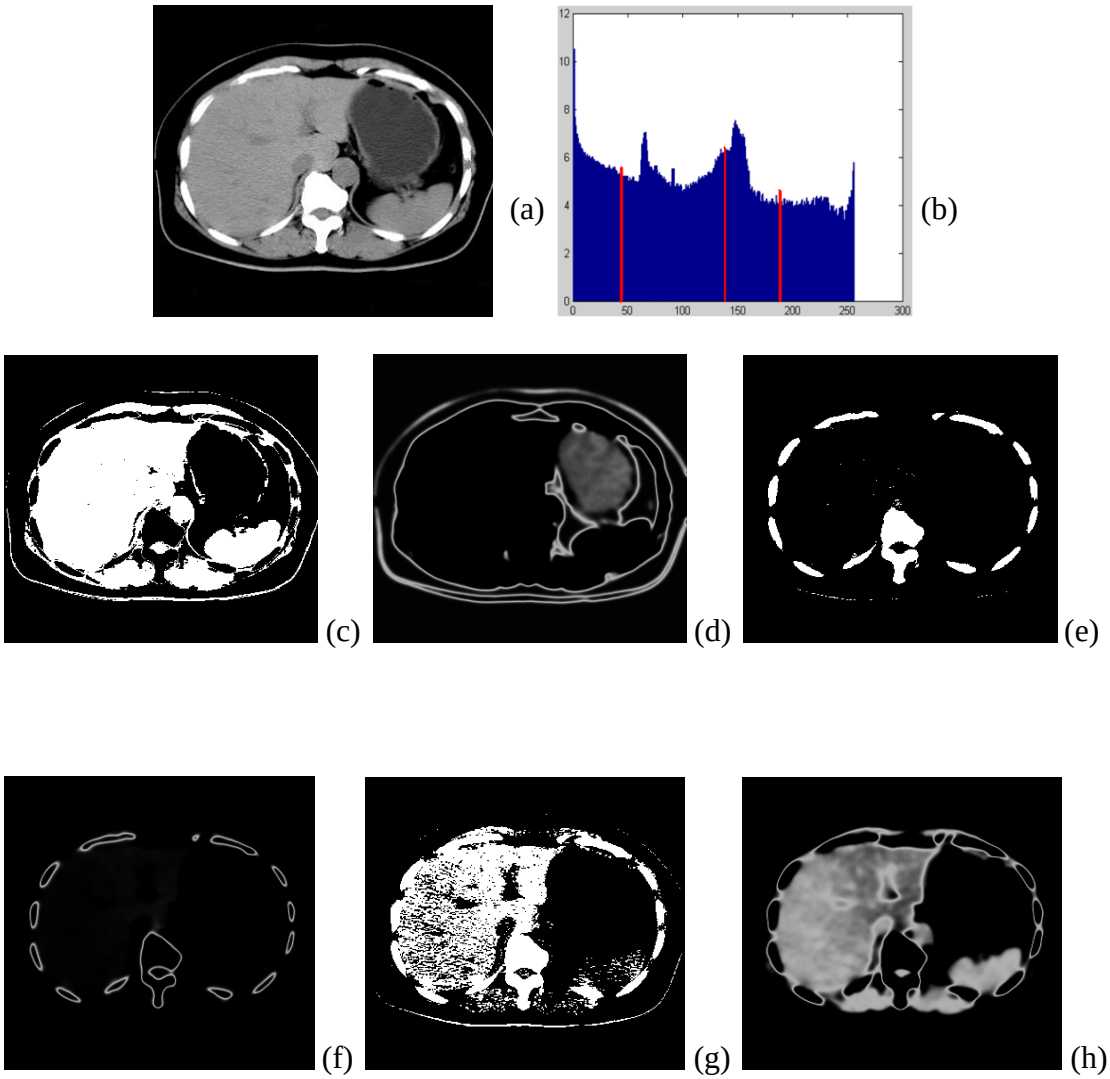

Figure. 2 An illustration of the class uncertainty theory. (a) A 2D image slice from a CT image of a patient's abdomen. (b) Image intensity histogram for (a) with three marks for thresholds , and . (c) The region computed by setting the threshold at . (d) The class uncertainty map computed for threshold at clearly depicting the tissue interface of lever and other soft tissues. (e,f) Same as (c,d) but for bone region with threshold at . (g,h) Same as (c,d) but using a threshold indicating no meaningful region. Note that the class-uncertainty map in (h) fails to indicate any tissue interface and spells over the entire soft tissue region.

Previously, Saha and Udupa [36] demonstrated the use of class-uncertainty and Postulate 1 for optimum threshold selection and later Saha et al. [37] showed its use for

improving the performance of a Snake-based segmentation algorithm. However, a major limitation of Saha and Udupa's work is that they used an ad hoc approach to computing a normalized measure for object boundaries which are coupled with class-uncertainty according to Postulate 1. Here, we aim to optimize the gradient parameter and use it to normalize the gradient map in the image. Further, this gradient parameter is not constant for all tissue interfaces. Here, we separately optimize the gradient parameter for each individual tissue interface.

2.1 Intensity-Based Class Uncertainty

Here, a digital image is represented as an ordered pair $\mathcal{C} = (C, f)$ whose first element specifies the image domain and the second element $f|C \longrightarrow [I_{MIN}, I_{MAX}]$, where I_{MIN} and I_{MAX} denote the minimum and maximum intensities, is the intensity function. Generally, C represents the points with integral co-ordinates those falling inside a hyper-rectangular parallelepiped. An element of C, commonly denoted as a vector **p**, **q** or **r** is called a pixel in two-dimension (2D); a voxel in three-dimension (3D) and a spel in n-dimension. Let $F_O \subset C$ and $F_B \subset C$ represent the hypothetical true object and background classes, respectively, in an image $\mathcal{C}$. Let $p_O(g)$ denote the *a priori* probability that an object spel possesses the intensity value , i.e.,

$$p_O(g) = P(f(\mathbf{p}) = g|\mathbf{p} \in F_O),$$

where P represents "probability". Similarly, let $p_B(g)$ denotes the *a priori* probability that a background spell has intensity value g, i.e.,

$$p_B(g) = P(f(\mathbf{p}) = g|\mathbf{p} \in F_B),$$

Independent of the intensity of a spel, let θ denote the probability of the spel belonging to the object class F_O so that $1-\theta$ is the probability of the spel belonging to the background class F_B. Often, θ is referred to as the density function. Therefore, the probability that any spel has the intensity value g, denoted by $p(g)$, is computed as follows

$$p(g) = \theta p_O(g) + (1-\theta)p_B(g)$$

Using the above equations, the *a posteriori* probability that a spel with intensity value g belongs to object class is defined using Bayes rule [7], i.e.,

$$P(\mathbf{p} \in F_O | f(\mathbf{p}) = g) = \frac{\theta p_O(g)}{p(g)},$$

Similarly, the *a posteriori* probability that a spel with intensity value g belongs to the background class is given by

$$P(\mathbf{p} \in F_B | f(\mathbf{p}) = g) = \frac{(1-\theta)p_B(g)}{p(g)}$$

The uncertainty measure of the classification that a spel $\mathbf{p} \in C$ with intensity value g falls into the object or background class is the entropy of the two *a posteriori* probability values as defined in Equations (6) and (7). This measure is referred to as class-uncertainty [36] and is estimated according to Shannon and Weaver's entropy equation [38] as follows:

$$h(g) = -\frac{\theta p_O(g)}{p(g)} \log \frac{\theta p_O(g)}{p(g)} - \frac{(1-\theta)p_B(g)}{p(g)} \log \frac{(1-\theta)p_B(g)}{p(g)}.$$

Here, the idea is to model the *a priori* probability distributions p_O and p_B and the density function θ as a function of the selected threshold t and the gradient parameter σ. Thus, the class-uncertainty map of an image varies as a function of threshold t and the

gradient parameter σ; and we will use $h_{t,\sigma}(g)\big|g \in [I_{MIN}, I_{MAX}]$ to denote the threshold and gradient-dependent class-uncertainty function. The methods for computing the *a priori* probability distributions p_O and p_B and the density function θ as a function of the selected threshold and gradient parameters t and σ are described in Chapter 3.

2.2 Energy Surface and Optimum Thresholding

Here, we use a normalized measure of image gradient to represent object boundaries as referred in Postulate 1. It's not difficult to find out from Equation (8) that class uncertainty measures are computed in the normalized [0,1] scale. Therefore, a meaningful formulation of the energy function as per Postulate 1 entails a normalized measure of image gradients. In other words, we need to introduce another gradient parameter σ into the optimization methods and, further, the parameter may not remain constant at different tissue interfaces. Here, we have adopted a Gaussian model to obtain a normalized measure ∇_σ of intensity gradients using the control parameter σ as follows:

$$\nabla_\sigma(\mathbf{p}) = 1 - e^{-\frac{(\nabla(\mathbf{p}))^2}{2\sigma^2}}$$

where ∇ is an intensity-gradient operator and ∇_σ is a normalized gradient operator. Note that the output of ∇ operator falls in the image intensity scale while that of the operator ∇_σ yields a gradient measure in the normalized scale of [0,1]. Finally, the energy function E is formulated as follows

$$E(t,\sigma) = \sum_{\mathbf{p}\in C} h_{t,\sigma}\big(f(\mathbf{p})\big) \times \big(1 - \nabla_\sigma(\mathbf{p})\big) + \Big(1 - h_{t,\sigma}\big(f(\mathbf{p})\big)\Big) \times \nabla_\sigma(\mathbf{p})$$

Following the above equation, each *spel* **p** contributes energies in two ways – (1) class uncertainty is high and gradient is low and (2) class-uncertainty is low and gradient

high. It may be noted that each of these two situations is a contradiction to Postulate 1. Therefore, the energy function E is formulated as an aggregate measure of contradictions of Postulate 1 from all spels in the image.

CHAPTER THREE

METHODS AND EXPERIMENTAL SETTING

3.1 Methods

Following the description in the previous chapter, the energy function E is controlled by two parameters, namely, the intensity threshold parameter t and the gradient parameter σ. It leads to an energy surface (see Figure. 5(e)) for the function E and the aim is to simultaneously optimize the two control parameters t and σ on that energy surface. In order to develop a threshold and gradient optimization algorithm based on the theory described in the previous chapter, for given values of t and σ, we need to compute – (1) *a priori* object and background intensity distributions $p_O(g)$ and $p_B(g)$, respectively, (2) density function θ, (3) normalized gradient map ∇_σ and (4) optimum values of t and σ on the energy surface E. In the following paragraphs, we describe the methods to accomplish each of these tasks.

At first, the original image is blurred using a Gaussian smoothing kernel [7], currently available under ITK application libraries [39]. The shape of the kernel (i.e., sharp or wide) is controlled by a standard deviation parameter σ_s and in the current implementation, we have used a constant value of two pixels/voxels for σ_s. This initial application of blurring serves two purposes. Firstly, it enhances regions with high class-uncertainty and smoothes out noise over homogeneous regions. As demonstrated by Saha and Udupa36, an image with sharp tissue interfaces leads to narrow regions with high class-uncertainty and may possess reduced power to control the overall energy function E. Secondly, the enhanced uncertainty map becomes more consistent with the enhancement

of the gradient map due to the blurring, often, used in a derivative of Gaussian (DoG) type edge operator [7]. Finally, it may be pointed out that optimum thresholds and gradients are applied on the original images. Therefore, the blurring used during the process of threshold and gradient optimization does not incur any structural loss or blurring at final segmentations.

According to the descriptions of Chapter 2, for any given values of the intensity threshold and gradient parameters t and σ, we compute *a priori* object and background intensity distributions $p_O(g)$ and $p_B(g)$ using the following equations.

$$p_O(g) = \begin{cases} 1 & \text{if } g > t + 1.5\sigma \\ e^{-\frac{(g-(t+1.5\sigma))^2}{2\sigma^2}} & \text{otherwise,} \end{cases}$$

and,

$$p_B(g) = \begin{cases} 1 & \text{if } g < t - 1.5\sigma \\ e^{-\frac{(g-(t-1.5\sigma))^2}{2\sigma^2}} & \text{otherwise.} \end{cases}$$

The motivation behind using $t + 1.5\sigma$ and $t - 1.5\sigma$ as reference object and background intensities is to dedicate a $3 \times \sigma$ intensity band (covering ~99.7% of population) for the interface between the object and background regions. It may be mentioned that, in Equation 11, the original intensity function f is replaced by the blurred image intensity function f_{Blur} while computing class uncertainty values. The density function θ is computed as the ratio of the number of spels in each of the two thresholded regions. The gradient map in the intensity scale is computed in 2D using the following equations

$$\nabla_{\text{x}}(\mathbf{p}) = f_{Blur}(\mathbf{p} + \mathbf{i}_{\text{x}}) - f_{Blur}(\mathbf{p} - \mathbf{i}_{\text{x}})$$
$$\nabla_{\text{y}}(\mathbf{p}) = f_{Blur}(\mathbf{p} + \mathbf{i}_{\text{y}}) - f_{Blur}(\mathbf{p} - \mathbf{i}_{\text{y}})$$
$$\nabla(\mathbf{p}) = \sqrt{\nabla_{\text{x}}^2(\mathbf{p}) + \nabla_{\text{y}}^2(\mathbf{p})}$$

where $\mathbf{i}_x$ and i_y are unit vectors along the x- and y-coordinate axes. The computation of the intensity gradient map immediately generalizes to 3D and to any higher dimension. Finally, the normalized gradient map is computed from the intensity gradient using Equation 9.

Now, we describe the optimization method for the threshold and gradient parameters t and σ. Following that the search space is only two-dimensional, we adopt an exhaustive search technique. Therefore, the most critical factor here is to define the geometry of optimum points on the energy surface. For the threshold parameter t, the entire intensity range $[I_{MIN}, I_{MAX}]$ is used for searching optimum locations. On the other hand, search-space for the gradient parameter σ is set to $[1\% \times (I_{MAX} - I_{MIN}), 40\% \times (I_{MAX} - I_{MIN})]$; we stay away from the extreme values of σ to reduce computation burden and to also to avoid computational instability. We determine two types of optimum locations on the energy surface – a Type I optimum location forms a meaningful pit on the energy surface E while a Type II optimum location forms a meaningful valley on E. Let E_σ denote energy function where the gradient parameter is fixed at a given value σ and the threshold parameter is varied; thus, E_σ forms an energy curve for the gradient parameter value σ. Local minimal on the energy surface E are referred to as pits while minima on an energy line E_σ are referred to as valley points. Depending upon the resolution of the search-space, both E and E_σ may contain a large number of noisy minima. Here, we use the idea of intrinsic basin, an idea similar to catchment basins used in watershed segmentation methods [40, 41], to distinguish between noisy and meaningful minima. Let (t_1, σ_1) denote a pit, i.e., a local minimal on the energy surface E. The intrinsic basin of (t_1, σ_1), denoted by $B(t_1, \sigma_1)$, is the set of all locations (t, σ) such that there exist a path from (t, σ) to (t_1, σ_1) and all points have energy values greater than equal to $E(t_1, \sigma_1)$. Essentially, $B(t_1, \sigma_1)$ corresponds to the region on E that can be flooded by pouring water from top at $E(t_1, \sigma_1)$ without water leaking to a location with energy value less than $E(t_1, \sigma_1)$ (see Figure. 3). In Figure. 3,

the black line denotes the energy line of intensity range $[I_{MIN}, I_{MAX}]$ at a certain gradient parameter σ_0, each color shows the intrinsic basin for that particular local minimum, and the depth of a basin is the distance from the top of one color to its bottom, while all red basins are counted as noise, invalid valley points.

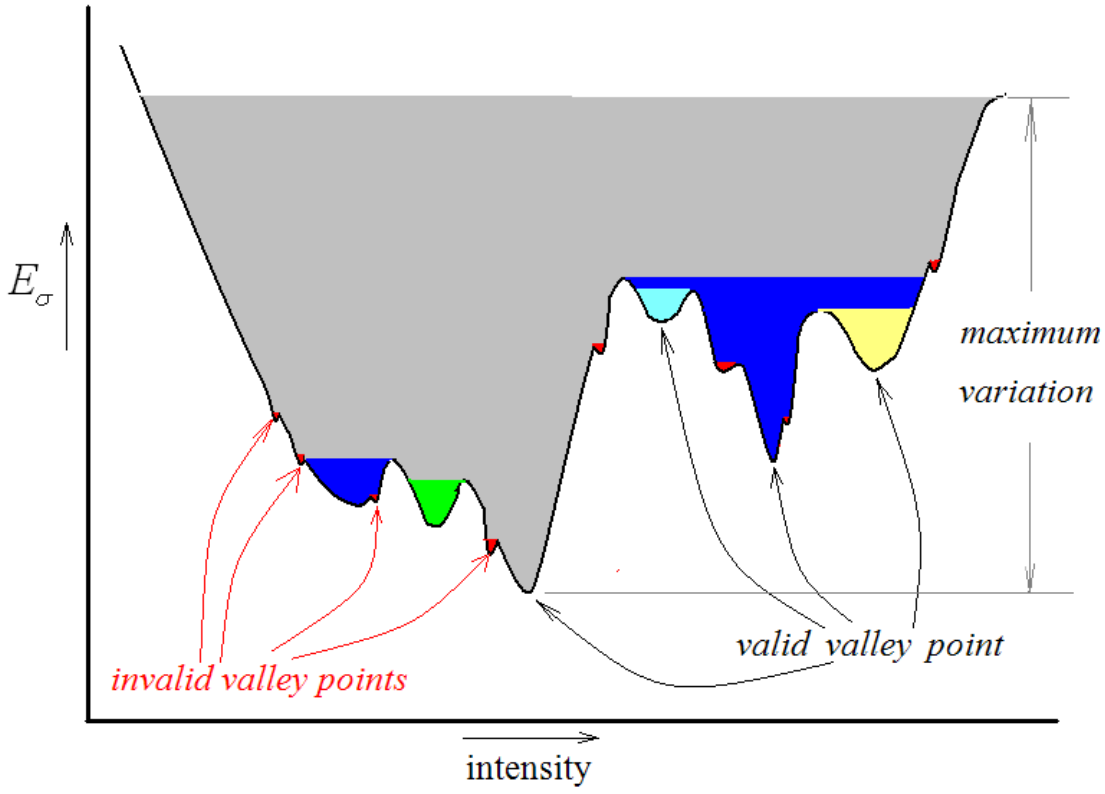

Figure. 3 An illustration of intrinsic basins.

An intrinsic basin $B_\sigma(t)$ for a valley point (t, σ), i.e., a local minima on the energy curve E_σ is defined similarly. A pit (or, a valley point) is considered as a valid pit (respectively, a valid valley point) if the height of $B(t_1, \sigma_1)$ (respectively, $B_\sigma(t)$) covers at least 3% of the maximum variation in E (respectively, E_σ). For example, the maximum variation in the energy curve E_σ is the depth of the grey basin. The depth of the tiny red

basins is less than 3% of the maximum variation and thus fails to quality as a valid valley. It has been observed from experimental studies that the both energy surfaces and curves formulated as above are mostly smooth with tiny fluctuations. Such fluctuations are more critical at flat regions of energy surfaces and curves. The primary motive of defining valid pits and valley points as above using intrinsic basins is to avoid such small fluctuations while capturing all meaningful minima. Each valid pit is identified as a Type I optimum location. A valley is defined as a connected path of valid valley points along the gradient parameter and a valley is a considered as a meaningful one if its length covers at least 10% of the search length along the gradient parameter. Finally, a Type II optimum point is defined at the center of a meaningful valley.

3.2 Experimental Setting

Here we describe our experimental plans to examine the effectiveness of the proposed thresholding method. Both 2D and 3D images from clinical scans and simulated 3D MR brain images available online at the Brainweb data site [42] have been used. Two dimensional images are used only for qualitative examinations while 3D images are used for both qualitative and quantitative evaluations. The overall aim of our experiments is to examine both accuracy and reproducibility of the proposed method. Both 3D CT images and simulated MR data sets are used for accuracy analysis while only CT images are used for reproducibility study.

3.2.1 CT image description

Two cadaveric ankle specimens were scanned in a Siemens Sensation 64 Multi-slice CT scanner at 120 kVp and 140 mAs to adequately visualize the bony structures. After scanning in a helical mode with a slice thickness of 0.6mm and collimation of $12 \times 0.6\text{mm}$, data was reconstructed at 0.3mm slice thickness with a normal cone beam method utilizing a very sharp algorithm of U75u to achieve high image resolution. Image

parameters for these scans were as follow: matrix size = 512×512 pixels; number of slice = 314; pixel size = 0.21mm. An image slice from one the CT scans is illustrated in Figure. 7(a). Each ankle specimen was scanned three times after repositioning on the table. These CT data sets have been used for examining both accuracy and reproducibility of the proposed method.

3.2.2 MR phantom image description

T1-weighted MR phantom images were generated at different levels of noise and slice thickness using the online facility supported by Brainweb site[42]. Specifically, four MR images were simulated at 0%, 1%, 3% and 5% noise levels and 1mm slice thickness and another phantom image was generated at 0% noise level and 3mm slice thickness. Image parameters for these images are as follows: matrix size = 181×217 pixels; number of slice = 181; voxel size = 1mm. Slices of these phantom images are illustrated in Figure. 8.

3.2.3 Error estimation

Two important questions need to be answered in order to quantitatively examine the accuracy of a thresholding method – (1) how to determine true thresholds and (2) how to estimate errors of a thresholding. We answer to the first question by using the mean of interactively selected thresholds by three human users. Let t denote the mean of the three thresholds separating two tissue regions selected by three users. Let s denote the automatically selected threshold separating the same tissue regions. The error of the thresholding is defined as follows

$$Error(s,t) = \frac{\sum_{i=s}^{t} H(i)}{\sum_{i=I_{MIN}}^{I_{MAX}} H(i)}$$

where $H(i)$ is the intensity histogram of the image; and the spirit behind the formulation of the error is graphically described in Figure. 4. When there are multiple

thresholds t_1, t_2 and t_3 for different tissue regions, the threshold t_i closest to s is selected for estimating the error.

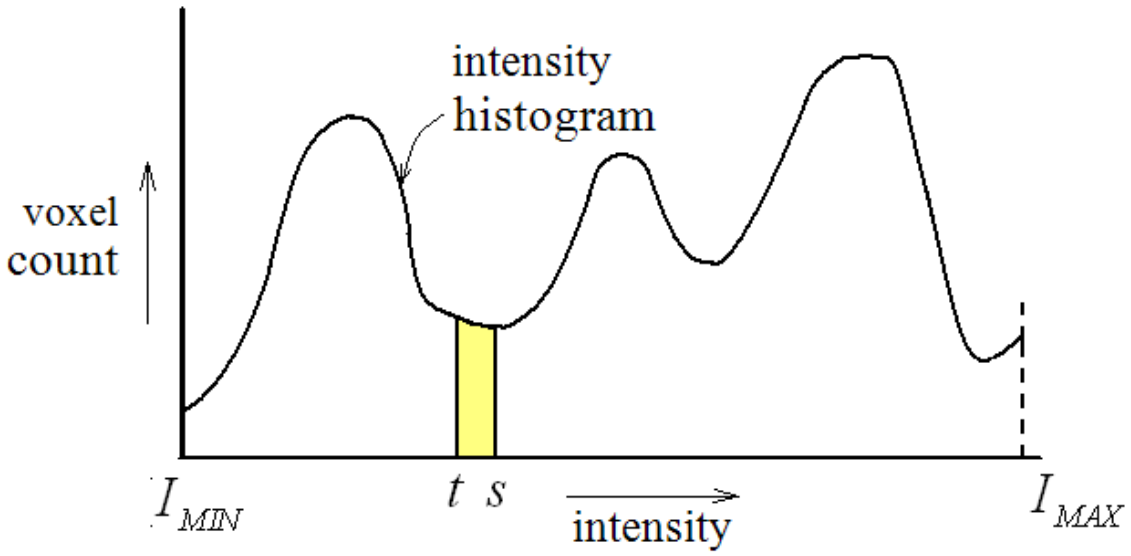

Figure. 4 A graphical description of the error function defining up the merit of a selected threshold s; here, t denotes the true threshold. Essentially, it computes the difference of the number of pixels/voxels, (the yellow region), normalized by image size.

CHAPTER FOUR

RESULT AND DISCUSSION

4.1 Results

4.1.1 Qualification analysis

Results of application of the method on 2D and 3D CT images are presented in Figure. 5-7, Figure. 5 illustrates the image slice from a CT image of lower abdomen constraining from different types of tissues, namely, bone, muscle, bladder and fat. The automatic thresholed selection method has successfully identified the four thresholds (see Figure. 5(c, d, e)). Figure. 5(d) denotes the four thresholded tissue region obtained from original image. Figure. 5(e) indicates the same applied on a smoothed image which clearly has less noise. More importantly, the class-uncertainty image at each optimized threshold describes the interfaces between respective tissue regions. Figure. 6 illustrates the results of application of the method on an image slice from a CT image of abdomen, Here, in the slice, four different tissue regions have been successfully identified. Also, the class-uncertainty imageas at different thresholds clearly depict the interfaces among corresponding tissue regions. Figure. 7 illustrates the results of application of the methods on 3D CT images of a cadaveric ankle where the thresholds separating the three different tissue regions (bone, muscle and fat) have been successfully detected.

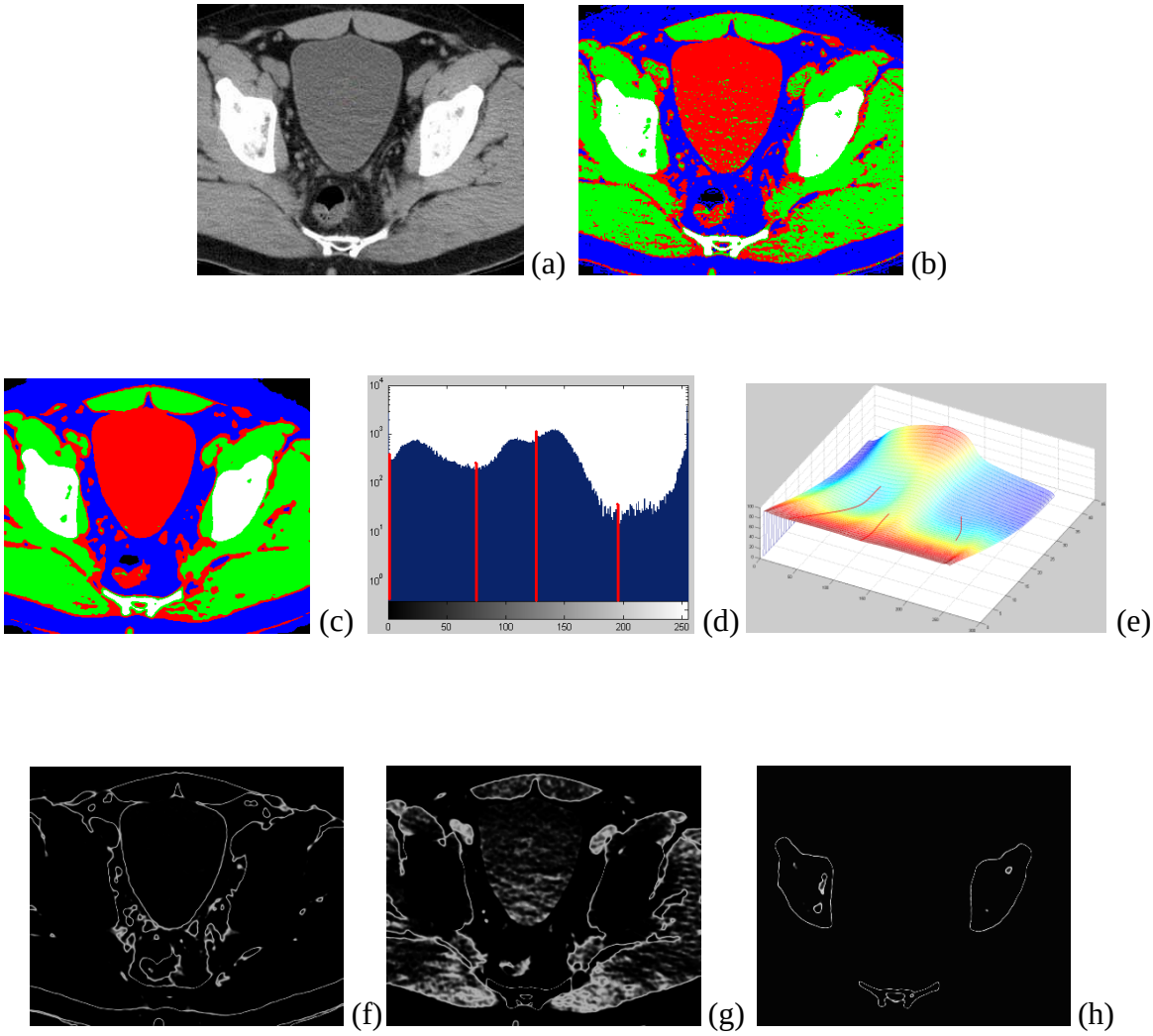

Figure. 5 Results of application of the method on an image slice from a CT data of lower abdomen. (a) Original CT image slice. (b) Thresholded regions in different colors as applied on the original image. (c) Same as (b) but applied on a smoothed image. (d) Thresholded regions in different colors as applied on the original image. (c) Same as (b) but applied on a smoothed image. (d) Thresholds shown in image histogram with red lines. (e) The energy surface/function with valley lines shown in red and pits indicated by red circles. (f-h) Object class uncertainty maps at different optimum thresholds. Note that the object class uncertainty image highlights different tissue interface at different optimum thresholds.

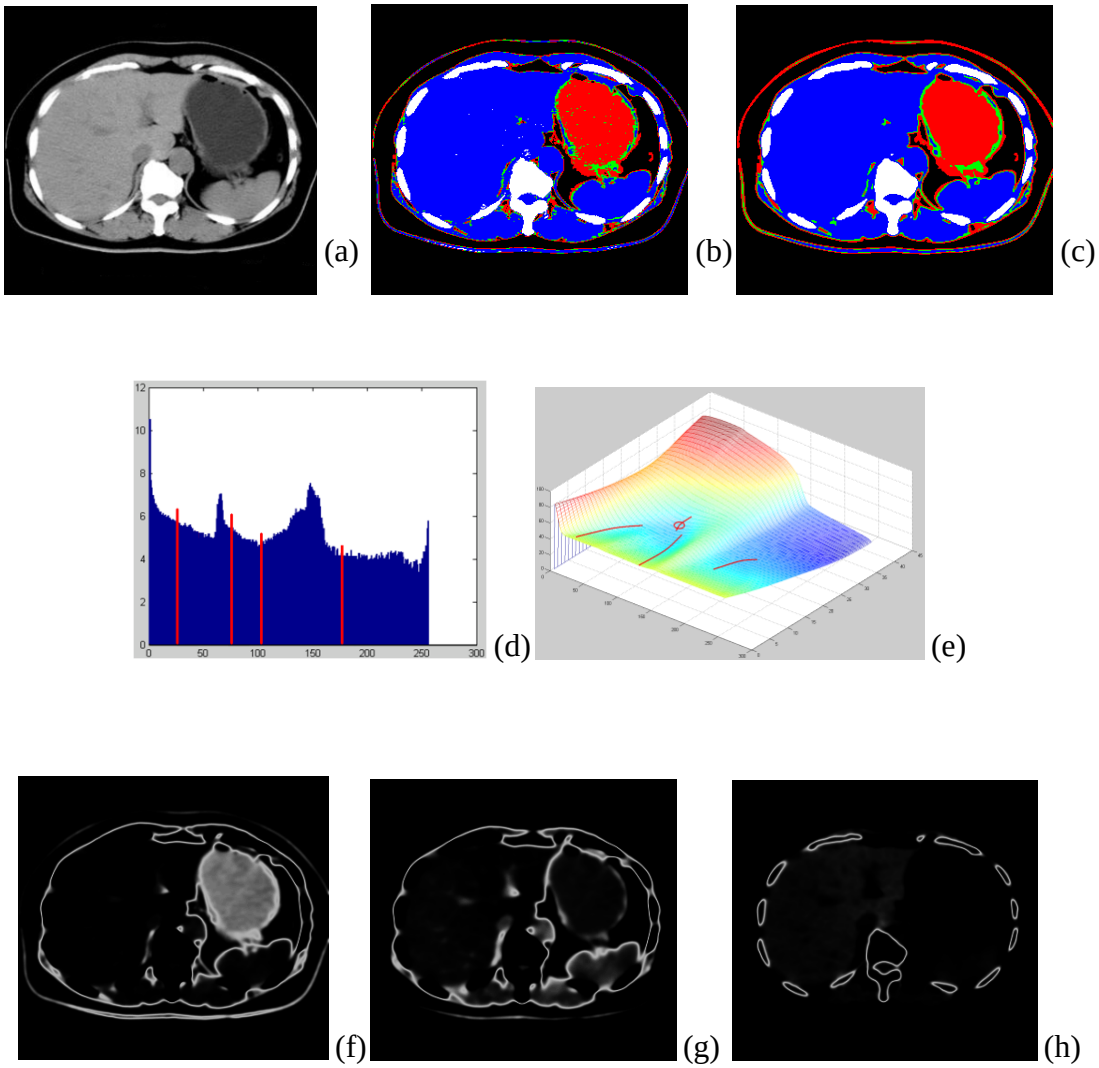

Figure. 6 Same as Figure. 5, but for a CT image slice of abdomen.

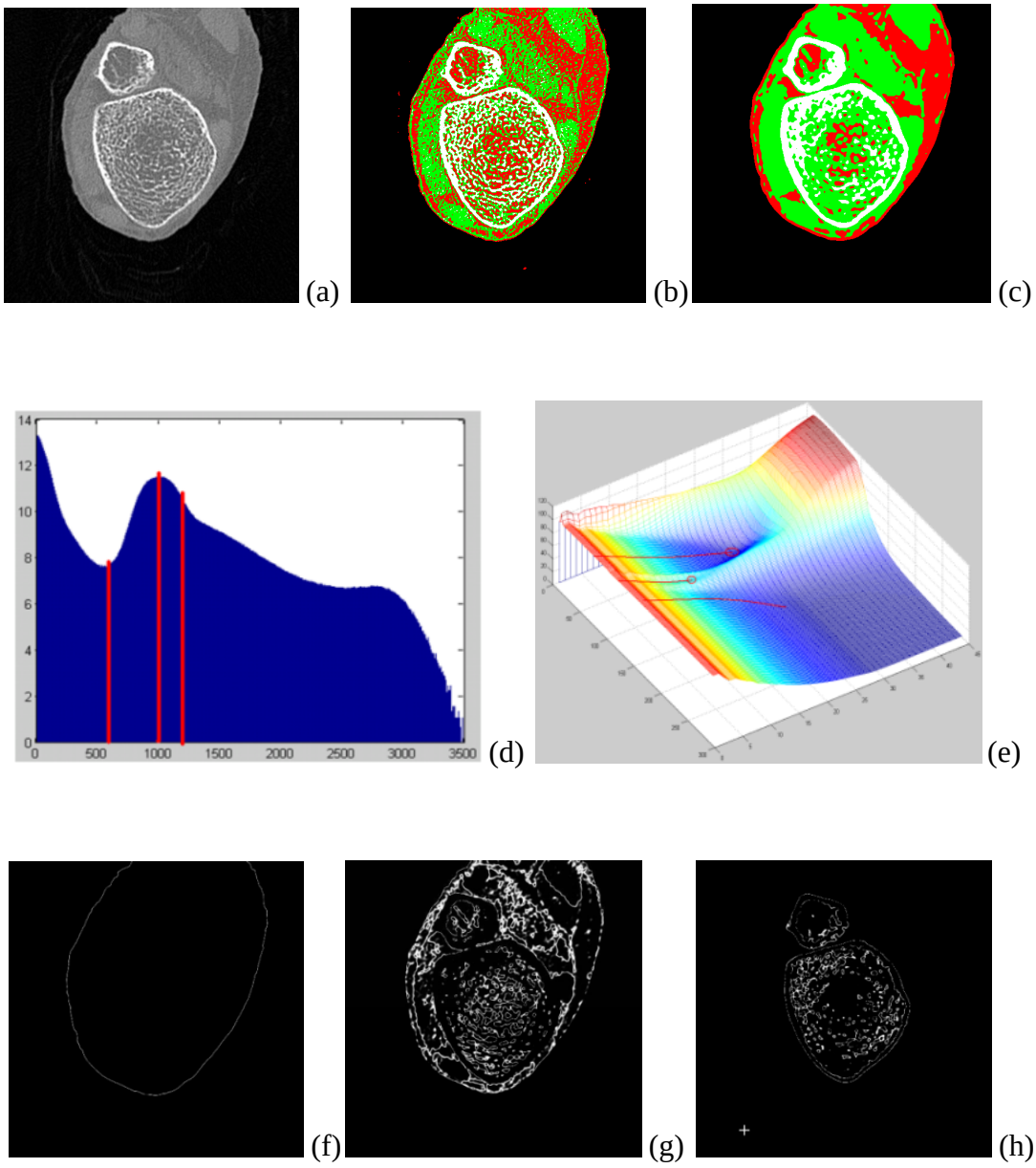

Figure. 7 Same as Figure. 5, but for a 3D CT image of ankle.

4.1.2 Comparison with Otsu's method

As an important thresholding method, Otsu's method is a nonparametric and unsupervised method of automatic threshold selection for picture segmentation is presented. An optimal threshold is selected by the discriminant criterion, namely, so as to maximize the separability of the resultant classes in gray levels. The procedure is very simple, utilizing only the zeroth- and the first-order cumulative moments of the gray-level histogram. [44]

Although proposed long time ago, Otsu's method is still a very popular thresholding method due to its simplicity and effectiveness, and extended Otsu's thresholding methods are also proposed in later years. Here the algorithm used do comparison is a multiple thresholding method, implemented in Insight Tool Kit [39].

This algorithm can find multiple thresholds as the user want; however, it can't automatically find proper number of thresholds for an image. So the comparison is done is the following way:

1). Use our automatic algorithm to determine how many thresholds should be found for the input image.

2). Do Otsu's thresholding with the number of thresholds obtained from above step.

3). Use different colors for different object regions.

Here, the image data used for comparison are gray-level images or 2d color images taken from nature scenes, all coming from internet but not clinical images. Figure. 8 shows the comparison result on gray-level 'Lena' image.

(a) (b) (c)

Figure. 8 Automatic thresholding compare with Otsu's thresholding method. (a) Original lena image. (b) Automatic thresholding result. (c) Otsu's threhsolding method with same number of thresholds

By comparing the two results, we can’t defeat one by another; however, one huge issue is that our new proposed method could automatically determine how many thresholds are needed for a certain image, while the Otsu’s method could not accomplish that by itself.

4.1.3 Accuracy analysis of MR phantom images

T1-weighted MR brain phantom images were used for quantitative accuracy analysis of the method. Here the ground truth is determined using manual thresholding of the noise free MR phantom image at 1mm slice thickness. For every image, both manual and automatic thresholding yields four thresholds separating each image into five regions; see Figure. 9 (e-h). A quantitative analysis of errors for different phantoms is presented in Table 1.

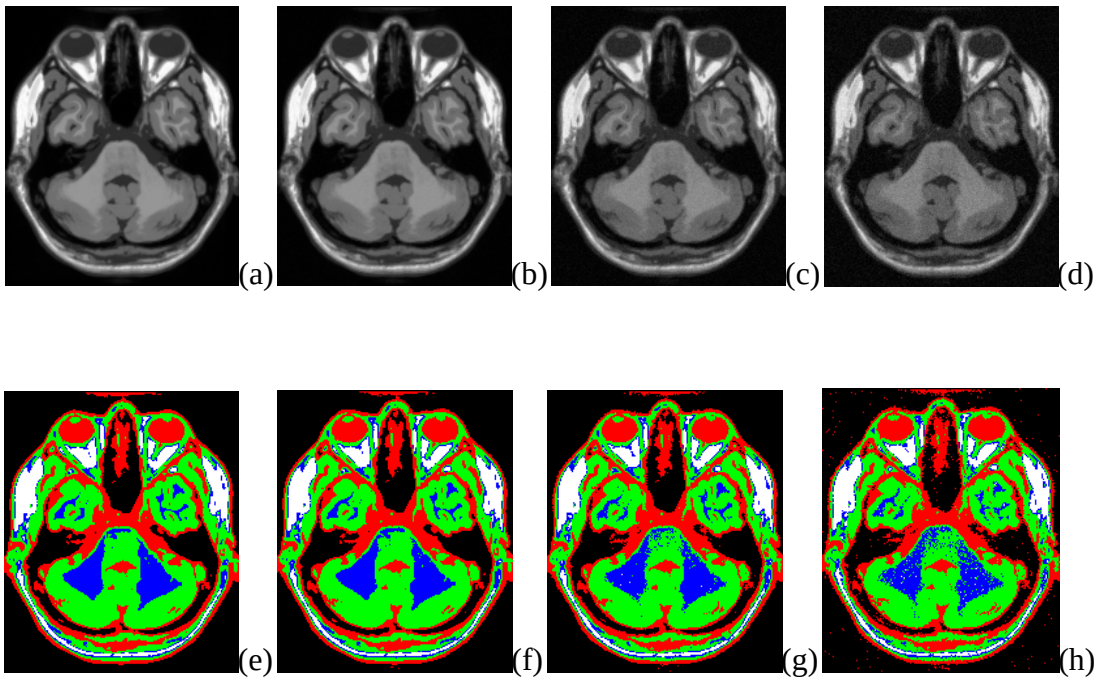

Figure. 9 MRI T1 phantoms with different noise levels and their segmented results. (a) no noise. (b) 1% noise. (c) 3% noise. (d) 5% noise. (e)-(g) segmented result for different noise levels.

Phantom description	Error rate			
	1st threshold	2nd threshold	3rd threshold	4th threshold
0% noise, 1mm	3.1%	3.0%	2.9%	3.4%
1% noise, 1mm	1.1%	0.7%	0.1%	0.2%
3% noise, 1mm	2.1%	2.0%	2.0%	2.3%
5% noise, 1mm	0.1%	0.1%	0.1%	0.001%
0% noise, 3mm	4.3%	3.1%	2.9%	0.1%

Table 1 Error measures of thresholding for different T1-weighted MR phantom images and tissue regions.

In Table 1, we can see that as noise level goes up, the thresholds will shift a little, higher noise level needs larger smoothing kernel size. And if the noise level goes even higher, some thresholds will disappear due to the merging of different brain regions.

4.1.4 Accuracy analysis on 3D CT ankle images

Threshold errors for CT images of cadaveric ankles are presented in Table 2. As mentioned previously, manual thresholding was used as the ground truth for thresholding. Here, three thresholds were identified for each CT image (see in Figure. 7). Table 2 presents the quantitative error measures of thresholding for the CT images of two ankle specimens.

Data description	Error rate		
	1st threshold	2nd threshold	3rd threshold
Ankle 1	0.1%	1.9%	0.7%
Ankle 2	0.2%	1.9%	0.8%

Table 2 Error measures of thresholding for T images of two ankle specimens.

4.1.5 Reproducibility analysis of 3D CT ankle image sets

For reproducibility analysis, we analyze the fractional volume of different tissue regions as computed by applying the proposed thresholding methods on CT images received by different scans. Table 3 shows these fractional volumes of different tissues in different scans. As shown in the table, varieties in thresholded tissue volumes vary minimally in different scans showing a high multi-scan reproducibility of the method.

	Image Dataset 1			Image Dataset 2		
	Bones	Tissue	Fat/Skin	Bones	Tissue	Fat/Skin
Data 1	21.1%	41.6%	37.3%	20.4%	44.0%	35.6%
Data 2	20.3%	41.8%	37.9%	20.5%	43.7%	35.8%
Data 3	20.2%	41.3%	38.5%	20.4%	44.2%	35.4%
Mean	20.5%	41.6%	37.9%	20.4%	44.0%	35.6%
Std. Dev.	0.45%	0.23%	0.57%	0.07%	0.24%	0.18%

Table 3 Preliminary results of reproducibility analysis using MDCT repeat scans of a cadaveric ankle specimen.

4.2 Discussion

A new method has been developed for simultaneously computing optimum values for thresholds and gradient parameters for different object/tissue interfaces. The method has been applied on several 2D and 3D medical image data sets and it has successfully determined both thresholds and gradients for different tissue interfaces even when some of the thresholds are almost impossible to locate in their histograms. Accuracy and reproducibility of the method have been evaluated using both MRI brain phantoms and real MDCT images of cadaveric ankles each scanned thrice and the preliminary results are very promising.

REFRENCES

[1] A. Rosenfeld and A. C. Kak, Digital Picture Processing I, vol. 1. Orlando, FL: Academic Press, Inc., 1982.

[2] A. Rosenfeld and A. C. Kak, Digital Picture Processing II, vol. 2. Orlando, FL: Academic Press, Inc., 1982.

[3] A. K. Jain, Fundamentals of Digital Image Processing. Upper Saddle River, NJ: Prentice Hall, 1989.

[4] J. K. Udupa and G. T. Herman, 3D Imaging in Medicine. Boca Raton, FL: CRC Press, 1991.

[5] R. C. Gonzalez and R. E. Woods, Digital Image Processing. Reading, MA: Addison-Wesley, 1992.

[6] J. C. Bezdek and S. K. Pal, Fuzzy Models for Pattern Recognition: Methods That Search for Structures in Data. New York, NY: IEEE, 1992.

[7] M. Sonka, V. Hlavac, and R. Boyle, Image Processing, Analysis, and Machine Vision. Pacific Grove, CA: PWS Publishing, 1999.

[8] R. N. Bracewell, Two-Dimensional imaging. Englewood Cliffs, New Jersey: Prentice-Hall, Inc., 1995.

[9] N. R. Pal and S. K. Pal, "A review of image segmentation techniques," Pattern Recognition, vol. 26, pp. 1277-1294, 1993.

[10] C. Johnson, R. MacLeod, and J. Schmidt, "Software tools for modeling, computation, and visualization in medicine," presented at Comp Med 94, 1995.

[11] M. Kass, A. Witkin, and D. Terzopoulos, "Snakes: active contour models," International Journal of Computer Vision, vol. 1, pp. 321-331, 1988.

[12] A. X. Falcão, J. K. Udupa, S. Samarasekera, and S. Sharma, "User-steered image segmentation paradigms: live wire and live lane," Graphical Models and Image Processing, vol. 60, pp. 233-260, 1998.

[13] J. K. Udupa, P. K. Saha, and R. A. Lotufo, "Relative fuzzy connectedness and object definition: theory, algorithms, and applications in image segmentation," IEEE Transactions on Pattern Analysis and Machine Intelligence, vol. 24, pp. 1485-1500, 2002.

[14] T. F. Cootes, C. J. Taylor, D. Cooper, and J. Graham, "Active shape models - their training and application," Computer Vision and Image Understanding, vol. 61, pp. 38-59, 1995.

[15] T. F. Cootes, G. J. Edwards, and C. J. Taylor, "Active appearance models," presented at European Conference on Computer Vision, 1998.

[16] P. K. Sahoo and S. Soltani, "A survey of thresholding techniques," Computer Vision Graphics Image Processing, vol. 41, pp. 233-260, 1988.

[17] S. U. Lee, S. Y. Chung, and R. H. Park, "A comparative performance study of several global thresholding techniques for segmentation," Computer Vision, Graphics, and Image Processing, vol. 52, pp. 171-190, 1990.

[18] C. A. Glasbey, "An analysis of histogram based thresholding algorithms," CVGIP: Graphical Models and Image Processing, vol. 55, pp. 532-537, 1993.

[19] J. Prewitt and M. Mendelsohn, "The analysis of cell images," Annals of the New York Academy of Sciences, vol. 128, pp. 1035-1053, 1966.

[20] W. Doyle, "Operations useful for similarity-invariant pattern recognition," Journal of the ACM, vol. 9, pp. 259-267, 1962.

[21] N. Otsu, "A threshold selection methods from grey-level histograms," IEEE Transactions on Pattern Analysis and Machine Intelligence, vol. 9, pp. 62-66, 1979.

[22] T. W. Ridler and S. Calvard, "Picture thresholding using an iterative selection method," IEEE Transactions on System, Man and Cybernetics, vol. 8, pp. 630-632, 1978.

[23] H. J. Trussell, "Comments on 'picture thresholding using an iterative selection method'," IEEE Transactions on Systems, Man and Cybernetics, vol. 9, pp. 311, 1979.

[24] W. H. Tsai, "Moment-preserving thresholding: A new approach," Computer Vision, Graphics, and Image Processing, vol. 29, pp. 377-393, 1985.

[25] T. Pun, "A new method for gray level picture thresholding using the entropy of the histogram," Signal Processing, vol. 2, pp. 223-237, 1980.

[26] A. K. C. Wong and P. K. Sahoo, "A gray-level threshold selection method based on maximum entropy principle," IEEE Transactions on Systems, Man and Cybernetics, vol. 19, pp. 866 - 871, 1989.

[27] N. R. Pal and S. K. Pal, "Entropy thresholding," Signal Processing, vol. 16, pp. 97-108, 1989.

[28] N. R. Pal and S. K. Pal, "Entropy: A new definition and its applications," IEEE Transactions on Systems, Man, and Cybernetics, vol. 21, pp. 1260-1270, 1991.

[29] J. N. Kapur, P. K. Sahoo, and A. K. C. Wong, "A new method for gray-level picture thresholding using the entropy of the histogram," Computer Vision, Graphics, and Image Processing, vol. 29, pp. 273-285, 1985.

[30] A. S. Abutableb, "Automatic thresholding of gray-level pictures using two-dimensional entropy," Computer Vision, Graphics, and Image Processing, vol. 47, pp. 22-32, 1989.

[31] A. Brink, "Maximum entropy segmentation based on the autocorrelation function of the image histogram," Journal of Computing and Information Technology, vol. 2, pp. 77-85, 1994.

[32] C. H. Li and C. K. Lee, "Minimum entropy thresholding," Pattern Recognition, vol. 26, pp. 617-625, 1993.

[33] J. Kittler and J. Illingworth, "Minimum error thresholding," Pattern Recognition, vol. 19, pp. 41-47, 1986.

[34] S. M. Dunn, D. Harwood, and L. S. Davis, "Local estimation of the uniform error threshold," IEEE Transactions on Pattern Analysis and Machine Intelligence, vol. 1, pp. 742-747, 1984.

[35] C. K. Leung and F. K. Lam, "Maximum segmented image information thresholding," Graphical Models and Image Processing,, vol. 60, pp. 57-76, 1998.

[36] P. K. Saha and J. K. Udupa, "Optimum threshold selection using class uncertainty and region homogeneity," IEEE Transactions on Pattern Analysis and Machine Intelligence, vol. 23, pp. 689-706, 2001.

[37] P. K. Saha, B. Das, and F. W. Wehrli, "An object class-uncertainty induced adaptive force and its application to a new hybrid snake," Pattern Recognition, vol. 40, pp. 2656-2671, 2007.

[38] C. E. Shannon and W. Weaver, The Mathematical Theory of Communication: University of Illinois Press, 1964.

[39] "ITK: The NLM Insight Segmentation and Registration Toolkit," in http://www.itk.org.

[40] P. Soille and M. Ansoult, "Automated basin delineation from DEMs using mathematical morphology," Signal Processing, vol. 20, pp. 171-182, 1990.

[41] L. Vincent and P. Soille, "Watersheds in digital spaces: An efficient algorithm based on immersion simulations," IEEE Transactions on Pattern Analysis and Machine Intelligence, vol. 13, pp. 583-598, 1991.

[42] "Brainweb: Simulated Brain Database," in http://www.bic.mni.mcgill.ca/brainweb/.

[43] Mehmet Sezgin and Bu¨ lent Sankur, "Survey over image thresholding techniques and quantitative performance evaluation," Journal of Electronic image, 13(1), pp.146-165, Jan 2004.

[44] Nobuyuki Otsu, "A Threshold Selection Method from Gray-Level Histograms," IEEE transactions on systems, man and cybernetics, Vol SMC-9, No.1, Jan 1979.